Evaluation of a Strategy for the Assimilation of Satellite Radiance Observations with the Local Ensemble Transform Kalman Filter

JOSÉ A. ARAVÉQUIA,* ISTVAN SZUNYOGH,+ ELANA J. FERTIG,# EUGENIA KALNAY,@ DAVID KUHL,& AND ERIC J. KOSTELICH**

* *Centro de Previsão de Tempo e Estudos Climáticos, São Paulo, Brazil*
+ *Texas A&M University, College Station, Texas*
# *John Hopkins University, Baltimore, Maryland*
@ *University of Maryland, College Park, College Park, Maryland*
& *Naval Research Laboratory, Washington, D.C.*
** *Arizona State University, Tempe, Arizona*

(Manuscript received 26 May 2010, in final form 4 November 2010)

ABSTRACT

This paper evaluates a strategy for the assimilation of satellite radiance observations with the local ensemble transform Kalman filter (LETKF) data assimilation scheme. The assimilation strategy includes a mechanism to select the radiance observations that are assimilated at a given grid point and an ensemble-based observation bias-correction technique. Numerical experiments are carried out with a reduced (T62L28) resolution version of the model component of the National Centers for Environmental Prediction (NCEP) Global Forecast System (GFS). The observations used for the evaluation of the assimilation strategy are AMSU-A level 1B brightness temperature data from the Earth Observing System (EOS) *Aqua* spacecraft. The assimilation of these observations, in addition to all operationally assimilated nonradiance observations, leads to a statistically significant improvement of both the temperature and wind analysis in the Southern Hemisphere. This result suggests that the LETKF, combined with the proposed data assimilation strategy for the assimilation of satellite radiance observations, can efficiently extract information from radiance observations.

1. Introduction

Although ensemble-based Kalman filter (EnKF) data assimilation schemes were first proposed more than a decade ago (Evensen 1994; Burgers et al. 1998; Houtekamer and Mitchell 1998) and several successful attempts at assimilating observations of the atmosphere have been reported in the last few years (e.g., Houtekamer et al. 2005; Whitaker et al. 2004, 2008; Szunyogh et al. 2008; Miyoshi and Sato 2007; Miyoshi and Yamane 2007; Torn and Hakim 2008; Bonavita et al. 2008), evidence has emerged only recently that EnKF schemes may be viable alternatives to the variational techniques in operational numerical weather prediction (e.g., Buehner et al. 2010a,b; Miyoshi et al. 2010).

In the present paper, we focus on the performance of one particular EnKF scheme, the local ensemble transform Kalman filter (LETKF), for assimilating satellite radiance observations. The LETKF algorithm was developed by Ott et al. (2004) and Hunt et al. (2004, 2007) and was tested on both simulated observations in the perfect-model scenario (Szunyogh et al. 2005) and on observations of the real atmosphere (Miyoshi and Sato 2007; Szunyogh et al. 2008; Whitaker et al. 2008). In particular, Szunyogh et al. (2008) and Whitaker et al. (2008) assimilated nonradiance observations in a reduced-resolution version of the model component of the National Centers for Environmental Prediction (NCEP) Global Forecast System (GFS) and found that the performance of the LETKF was superior to that of the Statistical Spectral Interpolation (SSI) of NCEP in data-sparse regions.[1]

Corresponding author address: José A. Aravéquia, Centro de Previsão de Tempo e Estudos Climáticos, Rodovia Dutra, km 40, CEP 12630-000, Cachoeira Paulista, São Paulo, Brazil.
E-mail: araveq@cptec.inpe.br

[1] The SSI was the operational three-dimensional variational (3D-Var) system of NCEP until April 2007.

DOI: 10.1175/2010MWR3515.1

Our goal here is to extend the study of Szunyogh et al. (2008) by augmenting the observational dataset with satellite radiance observations. To assimilate these satellite observations, we employ techniques for the localization and bias correction of the satellite radiance observations, which were developed and tested in an idealized setting in Fertig et al. (2007, 2009). The observations we assimilate are the Advanced Microwave Sounding Unit-A (AMSU-A) level 1B brightness temperature data from an instrument flown on the Earth Observing System (EOS) *Aqua* spacecraft (Olsen 2007). Hereafter, we refer to brightness temperature and radiance observations collectively as radiance observations, as the assimilation of both of these types of data requires the use of a radiative transfer model. The performance of the LETKF in assimilating radiance observations is assessed by comparing the results to those obtained by assimilating only the nonradiance observations.

Ours is not the first attempt at assimilating satellite radiance observations with an implementation of an EnKF scheme on a model of operational complexity: some studies assimilated satellite radiance observations using an offline estimate of the observation bias, which was provided by a variational data assimilation system (e.g., Houtekamer et al. 2005; Miyoshi and Sato 2007; Buehner et al. 2010b), while Miyoshi et al. (2010) combined the ensemble based estimation of the state with an online deterministic estimation of the observation bias. The unique aspect of our study is that it uses the ensemble-based approach to estimate both the bias and the state.

The structure of the paper is as follows. Section 2 provides a summary of our implementation of the LETKF on the model component of the NCEP GFS, while section 3 is a brief description of the AMSU-A observational datasets. Section 4 explains the design of our numerical experiments, whose results are reported in section 5. Section 6 offers a summary of our conclusions.

2. The LETKF for the NCEP GFS model

In what follows, we explain our implementation of the LETKF algorithm using the model component of the NCEP GFS. We introduce the major components of the data assimilation algorithm and summarize the data assimilation procedure for the conventional nonradiance observations. Then, we explain the modifications required to assimilate satellite radiance observations.

a. Definitions

We assume that, similar to the practice of operational numerical weather prediction, at the analysis time t_n, observations are assimilated from the observation time window:

$$\tau_n = (t_n - \Delta t/2,\ t_n + \Delta t/2).$$

The observations from τ_n form the vector of observations $\mathbf{y}_n^o$. In a typical global data assimilation system $\Delta t = 6$ h.

We introduce the notation $\boldsymbol{\gamma}_n$ for the state space trajectory of the model in τ_n:

$$\boldsymbol{\gamma}_n = \mathbf{x}(t), \quad t \in \tau_n, \tag{1}$$

where the vector $\mathbf{x}(t)$ is the finite-dimensional representation of the atmospheric state on the model grid. Similar to other ensemble-based data assimilation schemes, the LETKF algorithm prepares an ensemble of analyses, $\{\mathbf{x}_n^{a(k)}: k = 1, 2, \ldots, K\}$, based on the observation vector $\mathbf{y}_n^o$ and an ensemble of K analyses, $\{\mathbf{x}_{n-1}^{a(k)}: k = 1, 2, \ldots, K\}$, from the previous analysis time $t_{n-1} = t_n - \Delta t$. The associated computations consist of two main steps: the forecast step and the state-update step.

In the forecast step, a K-member ensemble of forecasts from time t_{n-1} to time $t_n + \Delta t/2$ is prepared using the analysis ensemble members $\{\mathbf{x}_{n-1}^{a(k)}: k = 1, 2, \ldots, K\}$, as initial conditions. This ensemble of forecasts provides an ensemble of model trajectories for the $3\Delta t/2$ long time period between t_{n-1} and $t_n + \Delta t/2$. The Δt-long section of the trajectories, which falls into τ_n provides the ensemble of background forecast trajectories, $\{\boldsymbol{\gamma}_n^{b(k)}: k = 1, 2, \ldots, K\}$. For instance, in our current implementation of the LETKF, the members of the background ensemble are 6-h forecast trajectories starting at the 3-h forecast lead time and ending at the 9-h forecast lead time relative to t_{n-1}. To obtain $\{\boldsymbol{\gamma}_1^{b(k)}: k = 1, 2, \ldots, K\}$ for the first analysis time, t_1, we use a random set of operational NCEP analyses valid at different times as the initial conditions $\{\mathbf{x}_0^{a(k)}: k = 1, 2, \ldots, K\}$.

The formulation of the state-update step of the LETKF, similar to that of all other modern data assimilation schemes, is based on the assumption that we know the observation operator $\mathbf{h}(\boldsymbol{\gamma}_n)$ that satisfies

$$\mathbf{y}_n^o = \mathbf{h}(\boldsymbol{\gamma}_n^{\text{true}}) + \boldsymbol{\varepsilon}_n, \quad t \in \tau_n. \tag{2}$$

Here, $\boldsymbol{\gamma}_n^{\text{true}}$ is the model representation of the (unknown) true system trajectory and $\boldsymbol{\varepsilon}_n$ is a vector of Gaussian random observation noise with zero mean and error covariance matrix $\mathbf{R}_n$. In practice, the observation operator, which operates on the background trajectories, typically consists of an interpolation of $\boldsymbol{\gamma}_n^b$ to the time and location of the observations and a conversion of the model variables to the observed physical quantities. In our implementation of the LETKF on the NCEP GFS, the time interpolation component of $\mathbf{h}(\boldsymbol{\gamma}_n^b)$ is performed by storing the background trajectories $\{\boldsymbol{\gamma}_n^{b(k)}: k = 1, 2, \ldots, K\}$ with

a 1-h resolution and applying a linear interpolation to the stored model fields to obtain the ensemble of model states at the observation times.

In what follows, we discuss how to obtain an ensemble of analyses at time t_n; thus, we can drop the subscript n from the notation without sacrificing clarity. In particular, we introduce the notation $\mathbf{x}^{b(k)}$ for the state at time t_n along the trajectory $\boldsymbol{\gamma}_n^{b(k)}$. LETKF obtains the different vector components of the members of the analysis ensemble independently for each grid point. We define a local state vector $\mathbf{x}_\ell$ that is composed of the model variables at model grid point ℓ. LETKF generates a K-member ensemble of local analyses, $\{\mathbf{x}_\ell^{a(k)}: k = 1, 2, \ldots, K\}$ by computing an ensemble of local "weight vectors," $\{\mathbf{w}_\ell^{(k)}: k = 1, 2, \ldots, K\}$ such that

$$\mathbf{x}_\ell^{a(k)} = \overline{\mathbf{x}}_\ell^b + \mathbf{X}_\ell^b \mathbf{w}_\ell^{(k)}, \quad k = 1, 2, \ldots, K. \tag{3}$$

Here, $\overline{\mathbf{x}}_\ell^b$ is the ensemble mean of the local background state vectors, $\{\mathbf{x}_\ell^{b(k)}: k = 1, 2, \ldots, K\}$, which are defined by the local components of the global background state vectors, $\{\mathbf{x}^{b(k)}: k = 1, 2, \ldots, K\}$. (Hereafter, the bar indicates the ensemble mean.) The kth column of the matrix of ensemble perturbations $\mathbf{X}_\ell^b$ is the kth local background ensemble perturbation defined by $\mathbf{x}_\ell^{b(k)} - \overline{\mathbf{x}}_\ell^b$. We estimate the state at location ℓ by the mean

$$\overline{\mathbf{x}}_\ell^a = \overline{\mathbf{x}}_\ell^b + \mathbf{X}_\ell^b \overline{\mathbf{w}}_\ell^a \tag{4}$$

of the analysis ensemble. The members of the global analysis ensemble, $\{\mathbf{x}^{a(k)}: k = 1, 2, \ldots, K\}$ are obtained by collecting the local analyses, $\{\mathbf{x}_\ell^{a(k)}: k = 1, 2, \ldots, K\}$. for all locations ℓ. We obtain the global estimate $\overline{\mathbf{x}}^a$ of the state by collecting the local ensemble mean analyses, $\overline{\mathbf{x}}_\ell^a$, for all locations ℓ.

b. Conventional observations

For the conventional (nonradiance) observations, the time interpolation component of the observation operator $\mathbf{h}(\boldsymbol{\gamma})$ is defined by the linear interpolation procedure described in section 2a, while in the two horizontal spatial dimensions, $\mathbf{h}(\boldsymbol{\gamma})$ is a bilinear interpolation. Since the vertical coordinate in the NCEP GFS model is σ (defined as the ratio of the pressure and the surface pressure) and the vertical position of the observations is given in pressure, the vertical interpolation for a given observation is carried out in three steps:

1) We calculate the pressure at each σ level at the horizontal location of the observation. This calculation requires the horizontal interpolation of the background surface pressure to the horizontal location of the observation and the multiplication of the results of the interpolation with σ at the given model level.
2) We define 28 σ layers, each bounded by a pair of σ levels (the lowest layer is defined by the model surface and the lowest σ level).
3) We find the σ layer that contains the observation and linearly interpolate the logarithm of the pressure to the vertical location of the observation based on the pressure values at the two σ levels that bound the layer.

We compute the local weight vectors $\{\mathbf{w}_\ell^{(k)}: k = 1, 2, \ldots, K\}$ and their ensemble mean $\overline{\mathbf{w}}_\ell$, which then provide the analysis ensemble and its mean through Eqs. (3) and (4), by the following procedure:

1) The observation operator $\mathbf{h}(\boldsymbol{\gamma})$ is applied to each member of the ensemble of background trajectories, $\{\boldsymbol{\gamma}^{b(k)}: k = 1, 2, \ldots, K\}$, to obtain an ensemble, $\{\mathbf{y}^{b(k)}: k = 1, 2, \ldots, K\}$, of the model-predicted values of the observables at the observation locations. The ensemble average $\overline{\mathbf{y}}^b$ of the ensemble $\{\mathbf{y}^{b(k)}: k = 1, 2, \ldots, K\}$ is computed and the matrix $\mathbf{Y}^b$ is constructed by taking its columns to be the vectors $\{\mathbf{y}^{b(k)} - \overline{\mathbf{y}}^b: k = 1, \ldots, K\}$.
2) The localization is performed. For each location (grid point) ℓ, the observations that are thought to have useful information about the atmospheric state at grid point ℓ are selected for assimilation. The selected observations form the local observation vector $\mathbf{y}_\ell^o$. The vector $\overline{\mathbf{y}}_\ell^b$ and the matrices $\mathbf{Y}_\ell^b$ and $\mathbf{R}_\ell$ are formed by selecting those vector components and matrix elements that are associated with the selected set of observations at ℓ. The sensitivity of the LETKF scheme to the localization parameters and the number of ensemble members was investigated in detail in Szunyogh et al. (2005). The issue was further investigated in Szunyogh et al. (2008), where it was found that, within a reasonable range, the accuracy of the analysis and the short-term forecasts was only weakly sensitive to the localization parameters. Here, we use the same localization parameters as in Szunyogh et al. (2008):
   (i) In the horizontal direction, observations are considered from an 800-km radius neighborhood of the location (grid point) ℓ. The influence of observations is tapered as a function of the radius r from the grid point. Formally, the tapering is achieved by multiplying $\mathbf{R}_\ell^{-1}$ by a factor $\mu(r)$: $\mu(r) = 1$ for $r \leq 500$ km and $\mu(r) = (800 - r)/300$ for 500 km $\leq r \leq$ 800 km.[2]

[2] This tapering function was introduced in Hunt et al. (2007) and tested in Szunyogh et al. (2008), where it was found that the tapering (i) had no effect on the accuracy of the analyses and the short-term forecasts in densely observed regions, but (ii) improved the accuracy in sparsely observed regions by making the spatial changes in the weight vector $\overline{\mathbf{w}}_\ell^a$ smoother.

(ii) In the vertical direction, observations are considered from a layer around ℓ. The depth of the layer is 0.35 scale height between model levels 1 and 15 (below $\sigma = 0.372$), and, starting with level 15, the depth gradually increases with height to reach 2 scale heights at the top of the model atmosphere (defined by $\sigma = 0.003$, which is equivalent to about 3 hPa). (The scale height is defined by the vertical distance in which the pressure drops by a factor of $e \approx 2.718$.) Surface pressure observations are also considered from the local horizontal region when the state is analyzed at a model grid point, which is at or below model level 15.

(iii) The surface pressure components of the state vector are treated differently from the other components. To obtain the surface pressure analysis at a location ℓ, we use all surface pressure observations from an 800-km radius of ℓ and all temperature and wind observations from an 800-km radius of ℓ between model levels 2 ($\sigma = 0.982$) and 5 ($\sigma = 0.916$). As for all other observation types, the influence of the surface pressure observations is tapered beyond a 500-km radius.

3) The weight vector $\overline{\mathbf{w}}_\ell$ is computed by

$$\overline{\mathbf{w}}_\ell = \mathbf{P}^a_\ell (\mathbf{Y}^b_\ell)^{\mathrm{T}} \mathbf{R}^{-1}_\ell (\mathbf{y}^o_\ell - \mathbf{y}^b_\ell). \tag{5}$$

In Eq. (5), $\mathbf{P}^a_\ell$ is the local analysis error covariance matrix, which is computed by

$$\mathbf{P}^a_\ell [(K-1)\mathbf{I}/\rho + (\mathbf{Y}^b_\ell)^{\mathrm{T}} \mathbf{R}^{-1}_\ell \mathbf{Y}^b_\ell]^{-1}. \tag{6}$$

Here, $\rho \geq 1$ is a multiplicative covariance inflation factor and $\mathbf{I}$ is the identity matrix. In our implementation, ρ is a smoothly varying three-dimensional scalar field: ρ tapers from 1.25 at the surface to 1.2 at the top of the model atmosphere in the SH extratropics and from 1.35 to 1.25 in the NH extratropics, while ρ changes smoothly throughout the tropics (between 25°S and 25°N) from the values of the SH extratropics to the values of the NH extratropics.

4) The matrix $\mathbf{W}_\ell$, whose columns are the local weight vectors for the ensemble perturbations, is computed by $\mathbf{W}_\ell = [(K-1)\mathbf{P}^a_\ell]^{1/2}$.

5) The weight vector $\overline{\mathbf{w}}_\ell$ is added to each row of $\mathbf{W}_\ell$. The columns of the resulting matrix are the members of the ensemble of weight vectors $\{\mathbf{w}^{(k)}_\ell : k = 1, \ldots, K\}$.

c. Satellite radiance observations

The assimilation procedure is more complicated for the radiance observations than for the conventional observations. The primary source of the added complexity is the observation operator $\mathbf{h}(\boldsymbol{\gamma})$, whose components for the radiance observations involve the use of a complex radiative transfer model, $\mathbf{T}(\boldsymbol{\gamma})$. For the radiance observations, $\mathbf{T}(\boldsymbol{\gamma})$ replaces the simple interpolation procedure described in step 1 of the LETKF algorithm. Since we follow different procedures for the radiance and the nonradiance observations, we decompose the observation operator into two components: $\mathbf{h}(\boldsymbol{\gamma}) = [\mathbf{h}^{(\mathrm{nr})}(\boldsymbol{\gamma}), \mathbf{h}^{(r)}(\boldsymbol{\gamma})]^{\mathrm{T}}$. The first component $\mathbf{h}^{(\mathrm{nr})}(\boldsymbol{\gamma})$ maps the state trajectory for the nonradiance observations and the component $\mathbf{h}^{(r)}(\boldsymbol{\gamma})$ maps the trajectory for the radiance observations.

The first challenge to be addressed is the correction of the bias in the radiance observations: the observation operator defined by $\mathbf{h}^{(r)}(\boldsymbol{\gamma}) = \mathbf{T}(\boldsymbol{\gamma})$ typically does not satisfy Eq. (2), because the observation error has a slowly varying, nonrandom component. To correct for this component of the error, we define the component of the observation operator for the radiance observations by

$$\mathbf{h}^{(r)}(\gamma) = \mathbf{T}(\gamma) + \mathbf{b}, \tag{7}$$

where $\mathbf{b}$ is the bias-correction term. The implementation of the observation operator defined by Eq. (7) requires a computational procedure to estimate $\mathbf{b}$. Following the general practice of numerical weather prediction (e.g., Eyre 1992; Derber and Wu 1998; Harris and Kelly 2001; Dee 2005), we make the estimation of $\mathbf{b}$ part of the data assimilation process. In particular, we assume that the $O^{(r)}$ components of $\mathbf{b}$ can be estimated by the linear combination

$$b_o(t) = \beta^0_o(t) + \sum_{i=1}^{I} \beta^i_0(t) p^i(t), \quad o = 1, 2, \ldots, O^{(r)}, \tag{8}$$

of a set of scalar predictors $\{p^i(t) : i = 1, \ldots, I\}$ [$O^{(r)}$ is the number of radiance observations]. Our task is to estimate the bias-correction parameters: $\{\beta^i_o : o = 1, 2, \ldots, O^{(r)}; i = 0, 1, 2, \ldots, I\}$.

The estimation of the $(I+1) \times O^{(r)}$ bias parameters is computationally not feasible, because in a typical NWP application $O^{(r)}$ is of order 10^6–10^8. To reduce the number of bias-correction parameters, we use the same set of predictors for all radiance observations, and assume that the bias-correction parameters are the same for all observations taken by a given instrument in a given channel. Thus, when the total number of channels we assimilate is J, the total number of bias-correction coefficients is $Q = (I+1) \times J$. These coefficients, $\{\beta^i_j : j = 1, 2, \ldots, J; i = 0, 1, 2, \ldots, I\}$ are the components of the vector of bias-correction coefficients β. When all predictors are zero, the bias correction for the jth channel is equal

to β_j^0. Thus, we refer to β_j^0 as the *intercept* for the jth channel. In addition, because the bias-correction procedure introduces a dependence of the observation operator on $\boldsymbol{\beta}$, for the radiance observations we write Eq. (7) as

$$\mathbf{h}^{(r)}(\boldsymbol{\gamma}, \boldsymbol{\beta}) = \mathbf{T}(\boldsymbol{\gamma}) + \mathbf{b}(\boldsymbol{\beta}). \tag{9}$$

With this notation Eq. (2) becomes

$$\mathbf{y}_n^o = \begin{bmatrix} \mathbf{y}^{o(\mathrm{nr})} \\ \mathbf{y}^{o(r)} \end{bmatrix} = \begin{bmatrix} \mathbf{h}^{(\mathrm{nr})}(\boldsymbol{\gamma}^{\mathrm{true}}) + \boldsymbol{\varepsilon}^{(\mathrm{nr})} \\ \mathbf{h}^{(r)}(\boldsymbol{\gamma}^{\mathrm{true}}, \boldsymbol{\beta}^{\mathrm{true}}) + \boldsymbol{\varepsilon}^{(r)} \end{bmatrix}, \tag{10}$$

where $\mathbf{y}^{o(\mathrm{nr})}$ is the vector of nonradiance observation and $\mathbf{y}^{o(r)}$ is the vector of radiance observations, while $\boldsymbol{\varepsilon}^{\mathrm{nr}}$ is the vector of random observation errors for the nonradiance observations and $\boldsymbol{\varepsilon}^r$ is the vector composed of the random part of the observation errors for the radiance observations.

The predictors $\{p^i(t)\colon i = 1, \ldots, I\}$ can be defined by any scalar physical parameters from the model or from the information provided with the observations (e.g., Eyre 1992; Derber and Wu 1998; Harris and Kelly 2001). Typical examples for model-based predictors are the skin temperature and the thickness of different atmospheric layers, while an example for an observation-related predictor is the scan angle at which the radiance observation is taken by the satellite-based observing instrument.

We obtain estimates of the bias parameters by the method of state augmentation (e.g., Friedland 1969; Derber and Wu 1998; Dee 2005), that is, we augment the state vector $\mathbf{x}$ by the Q components of $\boldsymbol{\beta}$ to obtain

$$\mathbf{z} = \begin{bmatrix} \mathbf{x} \\ \boldsymbol{\beta} \end{bmatrix}, \tag{11}$$

and apply the LETKF algorithm to the augmented state vector $\mathbf{z}$ instead of the state vector $\mathbf{x}$.

The method of state augmentation requires an equation to evolve $\boldsymbol{\beta}$ from one analysis time to the next. In our current implementation of the method, we evolve the bias parameters between two analysis times by assuming persistence of the bias parameters:

$$\left\{\beta_n^{b(k)} = \beta_{n-1}^{a(k)}\colon k = 1, 2, \ldots, K\right\}. \tag{12}$$

Using Eq. (12) in the forecast step of the analysis does not mean that the estimates of the bias-correction parameters cannot change with time. In fact, the state-update step typically changes the value of the bias parameters, that is,

$$\left\{\beta_n^{a(k)} \neq \beta_n^{b(k)}\colon k = 1, 2, \ldots, K\right\}, \tag{13}$$

which leads to

$$\left\{\beta_n^{a(k)} \neq \beta_{n-1}^{a(k)}\colon k = 1, 2, \ldots, K\right\}. \tag{14}$$

The second important issue is the nonlocal nature of the observation operator for radiance: in contrast to the case of the conventional observations, where the observation operator for a given observation depends on the model state only at the nearby grid points, the output of $\mathbf{T}(\boldsymbol{\gamma})$ depends on the entire atmospheric column of the model atmosphere. Thus, the vertical localization strategy, described in step 2 of the LETKF for the nonradiance observations, must be modified for the radiance observations (Fertig et al. 2007).

Our modified data selection strategy is based on the vertical weighting function ω_m, which is computed by $\mathbf{T}(\boldsymbol{\gamma})$ for each radiance observation at all model levels $m = 1, 2, \ldots, M$. For a given observation, $\mathbf{T}(\boldsymbol{\gamma})$ computes the radiance by

$$\mathbf{T}(\gamma) = \mathbf{R}_s + \sum_{m=1}^{M} B(T_m)\omega_m, \tag{15}$$

where $\mathbf{R}_s$ is the contribution of the earth's surface to the radiance, T_m is the temperature at model level m, $B(T_m)$ is the Planck function, and the weights $\{\omega_m\colon m = 1, 2, \ldots, M\}$ satisfy the following condition:

$$\sum_{m=1}^{M} \omega_m = 1. \tag{16}$$

We apply the cutoff-based observation strategy of Fertig et al. (2007) to select the model levels where a given observation is assimilated. In particular, we choose a cutoff parameter η ($0 < \eta \leq 1$), which we will use in step 3 of the data selection procedure below to determine the depth of the layer where the observation will be assimilated. (We use the same value of η for all channels.) We determine the layer for each observation in the following steps:

1) We apply $\mathbf{T}(\boldsymbol{\gamma})$ to all members of the ensemble of background trajectories $\{\boldsymbol{\gamma}^{b(k)}\colon k = 1, 2, \ldots, K\}$ to obtain an ensemble $\{\boldsymbol{\omega}_m^k : k = 1, 2, \ldots, K\}$ of the weight ω_m for the given observation.
2) We find the model level $m_{\max}^k$, where ω_m^k takes its maximum value $\omega_{\max}^k$ for each ensemble member.
3) We search for the top, m_{top}^k, and the bottom, m_{bottom}^k, of the deepest layer around level $m_{\max}^k$, in which the weighting function satisfies the condition $\omega_m^k \geq \eta\omega_{\max}^k$.

4) We compute the ensemble mean of the index of the top layers $\overline{m}_{\text{top}}$ and the ensemble mean of the index of the bottom layers, $\overline{m}_{\text{bottom}}$.
5) We assimilate the observations at model levels that fall into the layer bounded by $\overline{m}_{\text{bottom}}$ and $\overline{m}_{\text{top}}$.

An observation space localization approach, such as the one we have just described, may incorrectly eliminate correlations between the components of the background in observation space (between the components of the vectors that form $\mathbf{Y}^b$), unless all radiance observations associated with the correlated background errors in observation space are assimilated simultaneously at a given location l. The potential to incorrectly eliminate correlations is higher for the radiance than the conventional observations, because the neighboring satellite channels typically have broad overlapping weighting functions; thus, $\mathbf{T}(\boldsymbol{\gamma})$ may introduce significant correlations between model layers that are only weakly coupled by the dynamics (Campbell et al. 2010). The number of channels assimilated simultaneously is determined by η: the smaller the value of η, the more channels are assimilated simultaneously and the lower the chance that correlations are eliminated incorrectly. This argument is also supported by the results of Fertig et al. (2007), who showed that assimilating each radiance observation at multiple model levels, instead of the single level where ω_m^k takes its maximum value, resulted in more accurate analyses. Reducing the value of η, of course, increases the computational cost, because more observations are assimilated at each location. Thus, we determine the value of η by numerical experimentation, choosing a value of η, which is slightly smaller than the value at which the analysis and forecast accuracy starts to degrade noticeably.

To incorporate the bias estimation procedure into the LETKF, we define the observation operator for the radiance observations by Eq. 7, where $\mathbf{T}(\boldsymbol{\gamma})$ is the Community Radiative Transfer Model (CRTM; Han et al. 2006) of the Joint Center for Satellite Data Assimilation (JCSDA). In addition, we make the following specific changes in the main steps of the LETKF algorithm:

1) The ensemble of model-predicted radiance values at the observation locations is obtained by applying $\mathbf{h}^{(r)}$ to the background trajectories $\{\boldsymbol{\gamma}^{b(k)}: k = 1, \ldots, K\}$.
2) The horizontal localization is done the same way as for the conventional observations, while the vertical localization is done by the cutoff-based strategy. The components of the local augmented state vector $\mathbf{z}_\ell$ at location ℓ are the components of the local state vector $\mathbf{x}_\ell$, and the local vector of bias-correction parameters $\boldsymbol{\beta}_\ell$, which is composed of the bias-correction parameters for the channels that are assimilated at location ℓ. Steps 3–5 of the algorithm, which provide the weights $\mathbf{w}_\ell^{(k)}$ for the computation of the analysis of the local augmented state vector,

$$\mathbf{z}_\ell^{a(k)} = \overline{\mathbf{z}}_\ell^b + \mathbf{Z}_\ell^b \mathbf{w}_\ell^{(k)}, \tag{17}$$

are the same as for the conventional observations. The state analysis components $\{\mathbf{x}^{a(k)}: k = 1, 2, \ldots, K\}$ of $\{\mathbf{z}^{a(k)}: k = 1, 2, \ldots, K\}$ are obtained as before, collecting the state vector components $\mathbf{x}_\ell^{a(k)}$ of the local analyses of the augmented state vectors $\mathbf{z}_\ell^{a(k)}$for all locations ℓ. A different procedure is needed, however, to obtain the global analysis ensemble of bias parameters, $\{\boldsymbol{\beta}^{a(k)}: k = 1, \ldots, K\}$ from the bias-correction component, $\{\beta_\ell^{a(k)}: k = 1, \ldots, K\}$, of the local augmented state vectors, $\{\mathbf{z}_\ell^{a(k)}: k = 1, \ldots, K\}$. Because each component of the augmented state vector is estimated at many different locations ℓ, we need a computational strategy to obtain a single estimate of each of the Q bias parameters. We achieve this goal by averaging the local estimates of each bias parameter over all locations ℓ where it is estimated by the following formula:

$$\beta_q^{a(k)} = \frac{\sum_\ell \cos(\phi_\ell)\beta_{q,\ell}^{a(k)}\sigma_{q,\ell}^{-2}}{\sum_\ell \cos(\phi_\ell)\sigma_{q,\ell}^{-2}}, \quad q = 1, \ldots, Q. \tag{18}$$

Here, $\beta_q^{a(k)}$ and $\beta_{q,\ell}^{a(k)}$ are the qth components of $\boldsymbol{\beta}^{a(k)}$ and $\beta_\ell^{a(k)}$, respectively; ϕ_ℓ is the latitude at location ℓ; and the factor $\cos(\phi_\ell)$ accounts for the dependence on the latitude of the area represented by a grid point. The factor $\sigma_{q,\ell}^{-2}$ is the inverse of the variance,

$$\sigma_{q,\ell}^2 = (K-1)^{-1}\sum_{k=1}^{K}\left[\beta_{q,\ell}^{a(k)} - \overline{\beta}_{q,\ell}^a\right]^2, \tag{19}$$

of the analysis ensemble for the qth component of the bias parameter vector $\boldsymbol{\beta}$ at location ℓ. (Here, $\overline{\beta}_{q,\ell}^a$ is the ensemble mean analysis of the bias-correction parameter $\beta_{q,\ell}$ at location ℓ.) Weighting with the inverse of the variance ensures that locations where the uncertainty in the estimate of a given bias parameter is larger contribute with a smaller weight to the global estimate of that bias parameter.

3. The observations

Following the convention of operational numerical weather prediction for global models, we use a 6-h window and prepare analyses 4 times a day: at 0000, 0600, 1200, and 1800 UTC. A typical example for the number of

TABLE 1. Number of assimilated observations on a typical day (31 Jan 2004).

Assimilation cycle	0000 UTC	0600 UTC	1200 UTC	1800 UTC	Daily Tot
AMSU-A	34 694	35 131	35 794	36 133	141 752
Pressure	12 214	11 413	12 272	11 235	47 134
Temperature	44 424	17 325	39 385	26 060	127 194
Zonal wind	97 531	64 622	93 899	77 322	333 374
Meridional wind	97 948	64 911	94 256	77 373	334 488
Total	286 811	193 402	275 606	228 123	983 942

observations we assimilate is shown in Table 1.[3] On any given day, we assimilate about 1 million observations, of which about 15%–20% are radiance observations. These radiance observations fill important data voids in the coverage by the conventional data (see Figs. 1 and 2). We process many more observations than indicated by Table 1, but the number of observations is reduced by selecting only a subset of the radiance observations for assimilation and by rejecting observations that do not pass quality control. The data selection strategy and the quality control procedure are explained in section 4.

a. Conventional observations

We assimilate all conventional observations that were assimilated operationally at NCEP between 0000 UTC 1 January 2004 and 1800 UTC 29 February 2004. This dataset includes observations of the surface pressure by synoptic land stations; virtual temperature and surface pressure by surface marine observing platforms; splash-level virtual temperature by dropsondes; virtual temperature and wind by rawinsondes; sensible temperature and wind by commercial airliners; flight-level virtual temperature and wind by reconnaissance planes; cloud-drift wind by the *Meteorological Satellite-5* and *-7* (*Meteosat-5*) and (*Meteosat-7*), the *Geostationary Operational Environmental Satellite-8* and *-10* (*GOES-8*), and (*GOES-10*); and the Quick Scatterometer (QuikSCAT) surface wind by scatterometers. Figure 1 shows the spatial distribution of the assimilated temperature observations for a typical 6-h observation time window.

b. AMSU-A level 1B brightness temperature data

AMSU-A is primarily a temperature sounder that provides atmospheric information in the presence of nonprecipitating clouds. We assimilate a subset of the AMSU-A level 1B brightness temperature dataset, which contains calibrated and geolocated brightness temperatures in kelvin for 15 microwave channels. We assimilate only 8 of the 15 channels, since the observations from channels 1, 2, 3, and 15 have a strong surface signal component, while channels 12, 13, and 14 are strongly influenced by the atmospheric conditions at altitudes that are higher than the top of our model atmosphere. Figure 2 shows the spatial distribution of the assimilated AMSU-A observations for a typical 6-h observation time window.

The number of vertical levels used in the computation of the radiative transfer is one of the input parameters of the CRTM. After consulting colleagues with extensive experience with the CRTM, we decided to use 101 levels. Thus, in our implementation, the $\mathbf{h}^{(r)}(\boldsymbol{\gamma})$ observation operator for the AMSU-A observations involves

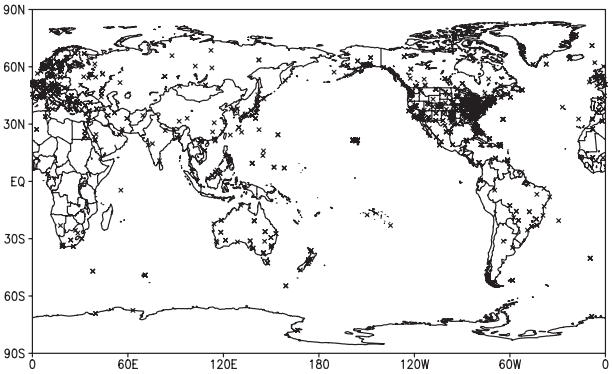

FIG. 1. Spatial distribution of the conventional temperature observations in a typical 6-h observation time window. The locations of the observations that were assimilated at grid points between σ levels 0.45 and 0.55, at 1200 UTC 15 Feb 2004, are marked by ×s. The total number of observation locations in this figure is 1415.

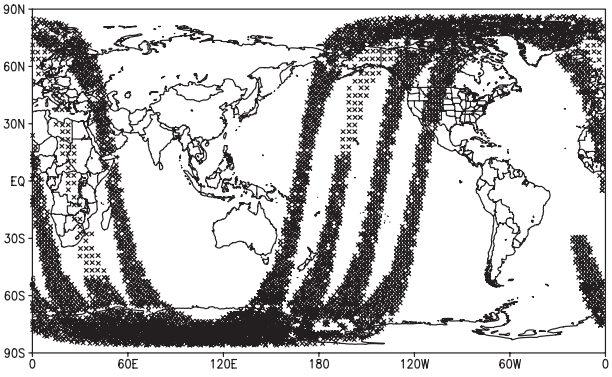

FIG. 2. Spatial distribution of the AMSU-A observations in a typical 6-h observation time window. The locations of the observations that were assimilated at 1200 UTC 15 Feb 2004 are marked by ×s. The total number of observation locations in this figure is 6394.

[3] The small (less than 0.5%) difference between the number of observations of the zonal and meridional components of the wind is a result of our approach of treating the two components of the wind as independent scalar variables in the data assimilation process (e.g., we perform quality control of the two wind components independently).

TABLE 2. AMSU-A channels selected for assimilation. The pressure level of peak sensitivity for each channel is shown for a randomly selected analysis time (1800 UTC 18 Feb 2004) at 2 particular locations (45°N and 45°S) along the date line.

AMSU channel No.	Peak at 45°N (hPa)	Peak at 45°S (hPa)
4	902	969
5	861	892
6	590	586
7	349	340
8	242	230
9	161	158
10	79	82
11	43	46

an interpolation of the background fields from the 28 model levels to the 101 levels used in the computation of the radiative transfer. Since the radiative transfer depends on the full atmospheric state, the maximum value of the weighting function, $\omega^k_{\max}$ and the pressure at the model level where ω^k_m takes that value, $\omega^k_{\max}$, are different at the different geographical locations and observation times. A couple of typical examples for the pressure values at which the different channels have the peak sensitivity according to the CRTM are shown in Table 2.

4. Numerical experiments

The primary goal of our numerical experiments is to determine how much improvement is achieved in the analyses when, in addition to the conventional observations, we assimilate the AMSU-A observations with the proposed strategy. We assess the performance of the data assimilation system when the AMSU-A observations are included by comparing the analysis and short-term (48 h) forecast errors with those from two reference experiments. In one of these reference experiments, we assimilate the AMSU-A observations but do not apply bias correction to the radiance observations, while in the other reference experiment, we assimilate only the conventional observations.

a. Experiment design

For the sake of computational efficiency, in the two experiments that assimilate radiance observations, we do not assimilate more than one radiance observation per channel at a given grid point. Instead, we assimilate the first observation from the dataset that satisfies all quality control criteria. In particular, we do not assimilate observations from mixed-surface footprints (e.g., from areas where seawater is mixed with ice), observations from channels 4 and 5 over land, and observations for which the scan angle is larger than 35°. We also reject observations for which the difference between the observed value and $\mathbf{h}(\boldsymbol{\gamma})$ is more than 5 times larger than both the ensemble spread (standard deviation of the ensemble) and the presumed standard error of the observations.

The model used in this study is the 2004 model component of the operational NCEP GSF truncated to T62L28 resolution. This model is identical to the one that was used in Szunyogh et al. (2008) and Whitaker et al. (2008). The only important improvement in our LETKF data assimilation system, compared to the one we evaluated in Szunyogh et al. (2008), is the correction of a coding error that led to the rejection of most scatterometer observations in the former implementation of the system. This correction leads to an improvement of the analyses and short-term forecasts in the Southern Hemisphere extratropics near the surface. We use this improved set of analyses as the baseline for the evaluation of the results obtained with the augmented observational dataset. Despite the aforementioned coding error, the former version of the LETKF provided analyses and short-term forecasts that in the SH, on average, were more accurate at the 99% significance level than those obtained with the then-operational SSI of NCEP at the same T62L28 resolution. Consequently, our baseline dataset consists of reasonably high quality analyses.

b. Verification methods

We verify analyses and forecasts on a 2.5° by 2.5° horizontal resolution grid at 16 standard pressure levels from 1000 to 10 hPa. We introduce the notation x^a and $x^f(\lambda_{g_\lambda}, \varphi_{g_\varphi}, p_{g_p}, t_i)$ for the state estimate (analysis or forecast) of an arbitrary scalar variable at the grid point located at longitude λ_{g_λ} ($g_\lambda = 1, 2, \ldots, 144$), latitude φ_{g_φ} ($g_\varphi = 1, 2, \ldots, 73$), and pressure level p_{g_p} ($g_p = 1, 2, \ldots, 16$) at time t_i ($i = 1, 2, \ldots, T$). Since we verify forecasts started from the 0000 and 1200 UTC analyses between 10 January and 27 February 2004, $T = 2 \times 49 = 98$. We measure the error in the state estimate at pressure level p_{g_p} and verification time t_i with the root-mean-square error:

$$E_{\mathrm{rms}}(p_{g_p}, t_i) = \left\{ \frac{1}{144 \times 73} \sum_{g_\lambda=1}^{144} \sum_{g_\varphi=1}^{73} [x^f(\lambda_{g_\lambda}, \varphi_{g_\varphi}, p_{g_p}, t_i) - x^v(\lambda_{g_\lambda}, \varphi_{g_\varphi}, p_{g_p}, t_i)]^2 \right\}^{1/2}. \quad (20)$$

In Eq. (20), $x^v(\lambda_{g_\lambda}, \varphi_{g_\varphi}, p_{g_p}, t_i)$ is a proxy for the true value of the scalar variable, which we define by the projection of the operational NCEP analysis at time t_i

onto the verification grid. Since the AMSU-A observations from the *Aqua* satellite were not assimilated by the operational NCEP analysis system,[4] and the algorithm used by the then-operational SSI data assimilation system of NCEP is substantively different from our LETKF algorithm, we have reason to believe that most of the changes we detect in the quality of the analyses are not due to correlation between the errors in $x^f(\lambda_{g_\lambda}, \varphi_{g_\varphi}, p_{g_p}, t_i)$ and $x^v(\lambda_{g_\lambda}, \varphi_{g_\varphi}, p_{g_p}, t_i)$.

We introduce the notation $\mathrm{ER}_{\mathrm{rms}}(p_{g_p}, t_i)$ for the root-mean-square error of the experiments that assimilate the AMSU-A observations and the notation $\mathrm{ENR}_{\mathrm{rms}}(p_{g_p}, t_i)$ for the root-mean-square error of the experiment that does not assimilate the AMSU-A observations. Likewise, we denote the sample mean of the root-mean-square error for the two experiments by $\mathrm{ER}_T(p_{g_p})$ and $\mathrm{ENR}_T(p_{g_p})$ where the sample mean is defined by the time mean:

$$E_T(p_{g_p}) = \frac{1}{T}\sum_{i=1}^{T} E_{\mathrm{rms}}(p_{g_p}, t_i). \tag{21}$$

We test the statistical significance of the difference between the time series of root-mean-square errors for the two configurations of the data assimilation system by testing the statistical significance of the difference between $\mathrm{ER}_T(p_{g_p})$ and $\mathrm{ENR}_T(p_{g_p})$ Our test is based on the two-sample t test for correlated data described in Example 5.2 of Wilks (2006). In particular, we define the time series,

$$\Delta(p_{g_p}, t_i) = \mathrm{ER}_{\mathrm{rms}}(p_{g_p}, t_i) - \mathrm{ENR}_{\mathrm{rms}}(p_{g_p}, t_i), \quad i = 1, 2, \ldots, T, \tag{22}$$

of the difference between the pairs of the root-mean-square-errors for the two experiments. The sample mean,

$$\Delta_T(p_{g_p}) = \frac{1}{T}\sum_{i=1}^{T}\Delta(p_{g_p}, t_i) = \mathrm{ER}_T(p_{g_p}) - \mathrm{ENR}_T(p_{g_p}), \tag{23}$$

is typically different from zero. The test computes the likelihood that the true mean of the random variable sampled by $\Delta(p_{g_p}, t_i)$ is also different from zero through the following steps:

1) The effective sample size

$$T'(p_{g_p}) \approx T[1 - r(p_{g_p})][1 + r(p_{g_p})]^{-1}, \tag{24}$$

is computed based on the assumption that $\Delta(p_{g_p}, t_i)$ describes a first-order autoregressive process. The autocorrelation coefficient $r(p_{g_p})$ is computed by

$$r(p_{g_p}) = \frac{\sum_{t=1}^{T-1}\left\{[\Delta(p_{g_p}, t) - \Delta_{\mathrm{T1}}(p_{g_p})][\Delta(p_{g_p}, t+1) - \Delta_{\mathrm{T2}}(p_{g_p})]\right\}}{\left\{\sum_{t=1}^{T-1}[\Delta(p_{g_p}, t) - \Delta_{\mathrm{T1}}(p_{g_p})]^2 \sum_{t=1}^{T}[\Delta(p_{g_p}, t+1) - \Delta_{\mathrm{T2}}(p_{g_p})]^2\right\}^{1/2}}. \tag{25}$$

Here, $\Delta_{\mathrm{T1}}(p_{g_p}) = (T-1)^{-1}\sum_{t=1}^{T-1}\Delta(p_{g_p}, t)$ and $\Delta_{\mathrm{T2}}(p_{g_p}) = (T-1)^{-1}\sum_{t=2}^{T}\Delta(p_{g_p}, t)$. If $r(p_{g_p})$ were zero, $T'(p_{g_p})$ would equal T, but as the autocorrelation increases, $T'(p_{g_p})$ decreases. [The sample size T has to be replaced by the effective sample size $T'(p_{g_p})$ because forecast errors at verification times separated only by 12-h tend to be strongly correlated.]

2) The test statistic

$$z(p_{g_p}) = \frac{\Delta_T(p_{g_p})}{[V_\Delta(p_{g_p})/T'(p_{g_p})]^{1/2}} \tag{26}$$

is computed, where $V_\Delta(p_{g_p})$ is the sample variance for the time series $V_\Delta(p_{g_p}, t)$, t=1, 2, ..., T). Under the assumption that both time series of root-mean-square errors sample normally distributed random processes, when the true mean of the random process sampled by $\Delta(p_{g_p}, t)$ is zero, the random variable z is normally distributed with standardized statistics.

3) The likelihood l that the particular value of z we obtain for a given set of analysis or forecast errors is from a standardized normal distribution is determined (e.g., with the help of a table of cumulative probabilities for the standardized normal distribution).

4) The difference between the accuracy of the forecasts for the two configurations is deemed statistically significant at the $(1 - L)$ level, if $l \le L$. For instance, the difference between the two time series of root-mean-square errors is statistically significant at the 99% level if $\|z\| \ge 2.58$ and only at the 90% level if $\|z\| \ge 1.65$.

[4] In 2004 NCEP assimilated AMSU-A observations from the *NOAA-15* and *NOAA-16* satellites.

We prepare two types of figures to investigate the spatial distribution of the forecast improvements (degradations). In the first type of figure, we show the horizontal distribution of the forecast improvements (degradations). To obtain such figures, we first compute the square error,

$$E_s(\lambda_{g_\lambda}, \varphi_{g_\varphi}, p_{g_p}, t_i) = [(x^f(\lambda_{g_\lambda}, \varphi_{g_\varphi}, p_{g_p}, t_i) - x^v(\lambda_{g_\lambda}, \varphi_{g_\varphi}, p_{g_p}, t_i)]^2, \quad (27)$$

for each grid point $(\lambda_{g_\lambda}, \varphi_{g_\varphi}, p_{g_p})$ and verification time t_i. Then, we compute

$$E_{\rm ms}(\lambda_{g_\lambda}, \varphi_{g_\varphi}, p_{g_p}) = \frac{1}{T}\sum_{i=1}^{T} E_s(\lambda_{g_\lambda}, \varphi_{g_\varphi}, p_{g_p}, t_i) \quad (28)$$

at each grid point for both experiments. We denote the value of $E_{\rm ms}(\lambda_{g_\lambda}, \varphi_{g_\varphi}, p_{g_p})$ for the two experiments by $\mathrm{ER}_{\rm ms}(\lambda_{g_\lambda}, \varphi_{g_\varphi}, p_{g_p})$ and $\mathrm{ENR}_{\rm ms}(\lambda_{g_\lambda}, \varphi_{g_\varphi}, p_{g_p})$ and compute the improvement (degradation) due to the assimilation of the AMSU-A data by

$$I(\lambda_{g_\lambda}, \varphi_{g_\varphi}, p_{g_p}) = \frac{\mathrm{ER}_{\rm ms}(\lambda_{g_\lambda}, \varphi_{g_\varphi}, p_{g_p}) - \mathrm{ENR}_{\rm ms}(\lambda_{g_\lambda}, \varphi_{g_\varphi}, p_{g_p})}{\left|\mathrm{ER}_{\rm ms}(\lambda_{g_\lambda}, \varphi_{g_\varphi}, p_{g_p}) - \mathrm{ENR}_{\rm ms}(\lambda_{g_\lambda}, \varphi_{g_\varphi}, p_{g_p})\right|^{1/2}}. \quad (29)$$

The symbol $|\cdot|$ stands for the absolute value. The magnitude of $I(\lambda_{g_\lambda}, \varphi_{g_\varphi}, p_{g_p})$ is equal to the square root of the difference between the mean-square error of the two experiments and its sign is negative at locations of improvement $[\mathrm{ER}_{\rm ms}(\lambda_{g_\lambda}, \varphi_{g_\varphi}, p_{g_p}) < \mathrm{ENR}_{\rm ms}(\lambda_{g_\lambda}, \varphi_{g_\varphi}, p_{g_p})]$ and positive at locations of degradation $[\mathrm{ER}_{\rm ms}(\lambda_{g_\lambda}, \varphi_{g_\varphi}, p_{g_p}) > \mathrm{ENR}_{\rm ms}(\lambda_{g_\lambda}, \varphi_{g_\varphi}, p_{g_p})]$ To filter $I(\lambda_{g_\lambda}, \varphi_{g_\varphi}, p_{g_p})$ based on the statistical significance, we follow the procedure described for the root-mean-square error, except that we define the time series of differences by $(\lambda_{g_\lambda}, \varphi_{g_\varphi}, p_{g_p}, t_i)\mathrm{ER}_s(\lambda_{g_\lambda}, \varphi_{g_\varphi}, p_{g_p}) - \mathrm{ENR}_s(\lambda_{g_\lambda}, \varphi_{g_\varphi}, p_{g_p}, t_i)$.

c. LETKF parameters

Most of our choices of the LETKF parameters, which define the localization for the conventional observations and the variance inflation for the state vector components, are discussed in section 2. Since observation density has a large influence on the optimal level of variance inflation (e.g., Satterfield and Szunyogh 2011), retuning the variance inflation factor, ρ, for the configurations of the data assimilation system, which assimilate the AMSU-A observations, would likely lead to a further increase of the accuracy of the analyses and the ensuing forecasts. Notwithstanding the potential positive effects of retuning ρ on the accuracy of the analyses in the experiment that assimilates the AMSU-A observations, for the sake of a conservative comparison to the results of the reference experiments, we opt not to retune ρ.

We find that the ensemble of bias-correction parameters collapses for some of the bias parameters unless we apply an additional inflation, with coefficient $\rho_\beta > 1$, to the $\{\beta_q^{a(k)} - \overline{\beta}_q^{a(k)}: k = 1, 2, \ldots, K; q = 1, 2, \ldots, Q\}$ bias-correction components of the analysis ensemble perturbations. We also find that by applying $\rho_\beta = 1.07$ to the ensemble perturbations of all Q bias parameters, we can avoid a collapse of the ensemble for all Q bias parameters.

The radiance observations are corrected using two predictors: the skin temperature (p_1) and the scan angle (p_2), that is, the bias-correction term is estimated by

$$b_j\beta_j^0 + \beta_j^1 p_1 + \beta_j^2 p_2, \quad j = 1, \ldots, J = 8. \quad (30)$$

Since we estimate all bias parameters adaptively[5] and the number of bias parameters for each channel is $(I + 1) = 3$, the total number of bias parameters that we estimate is $Q = (I + 1) \times J = 24$. The areal average values of the bias-correction parameters are obtained from the local values by averaging them over all observation locations in three zonal latitude bands (90°–30°S, 30°S–30°N, 30°–90°N) using Eqs. (18) and (19). We chose this particular set of predictors and averaging regions based on a large number of numerical experiments with different predictors suggested in the literature. We define the initial value of the estimates of the Q bias parameters by a set of random samples from a standardized normal distribution.

We find that a 60-member ensemble provides a sufficiently large number of degrees of freedom to obtain accurate estimates of the bias parameters and the atmospheric state. We also find that a cutoff value of $\eta = 0.8$ provides a performance that is similarly good to that for lower values, but at a lower computational cost.

5. Results

a. Analysis and forecast verification results

Figures 3 and 4 show the time evolution of the root-mean-square error $E_{\rm rms}(p_{g_p}, t_i)$ $(i = 1, 2, \ldots, T)$, for the analysis of the temperature and the meridional component of the wind at three atmospheric levels in the SH extratropics. The results indicate that the assimilation of the radiance observations with our strategy improves the analysis and forecast not only of the temperature,

[5] We note that some organizations (e.g., NCEP) estimate the scan angle bias predictor by a separate offline procedure.

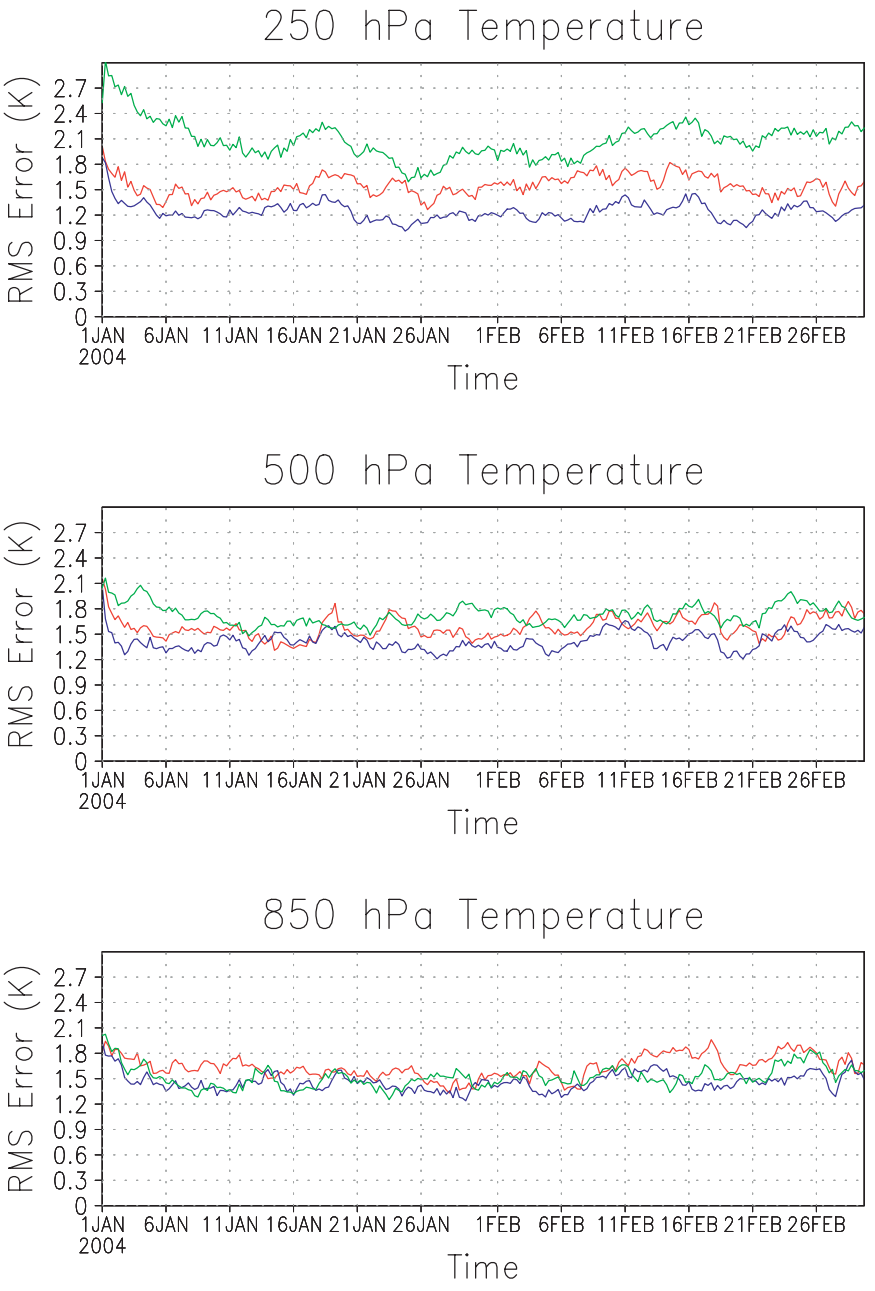

FIG. 3. Time evolution of the root-mean-square error $E_{\mathrm{rms}}(p_{g_p}, t_i)$ $(i = 1, 2, \ldots, T)$, for the temperature analysis at three different model levels in the SH. Shown are the results with the satellite radiance observations using bias correction (blue), with the satellite radiance observations not using bias correction (green), and without satellite radiance observations (red).

which is the model variable most closely related to the radiance through the observation operator, but also of the two horizontal components of the wind. This result suggests that the ensemble-based estimate of the cross correlation between the errors in the background temperature and wind is sufficiently accurate to lead to an improvement of the wind analysis. Figures 3 and 4 also show that the bias correction has a larger positive effect in the upper troposphere than in the lower troposphere and that employing a bias-correction scheme is especially important for the temperature analysis to benefit from the AMSU-A observations.

We show the time series of root-mean-square error only for the SH extratropics because this is the region

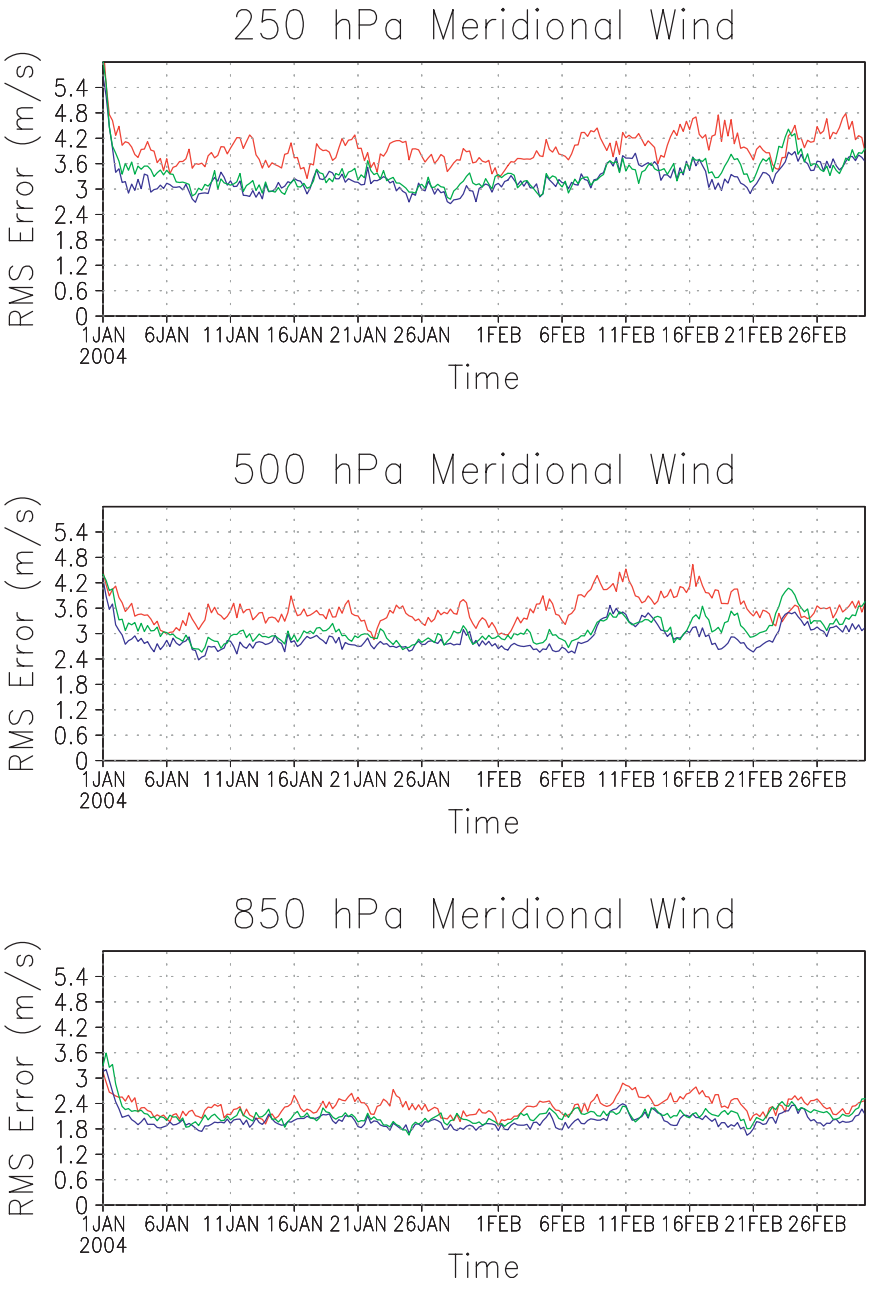

FIG. 4. As in Fig. 3, but for the meridional component of the wind instead of the temperature.

where the difference between the time series from the different experiments is statistically highly significant (at the 99% at most pressure levels). The full vertical profile of $E_T(p_{g_p})$ is shown at both analysis and 48-h forecast time for the SH and the NH extratropics, respectively, in Figs. 5 and 6. These figures show that the bias correction has a large positive impact on the analysis and forecast accuracy in the upper troposphere and the stratosphere. Interestingly, when the bias is not corrected, we observe a large degradation instead of the large improvement in the same atmospheric region due to the assimilation of the AMSU-A observations. In addition, Fig. 5 also shows that the assimilation of AMSU-A observations leads to an improvement of the analyses and the forecasts in the lower troposphere in the SH extratropics even without bias correction.

The geographical distribution of the improvement in the 48-h forecasts is shown in Figs. 7 and 8. The only difference between these two figures is that, in Fig. 8, the difference between the forecast errors is not shown at

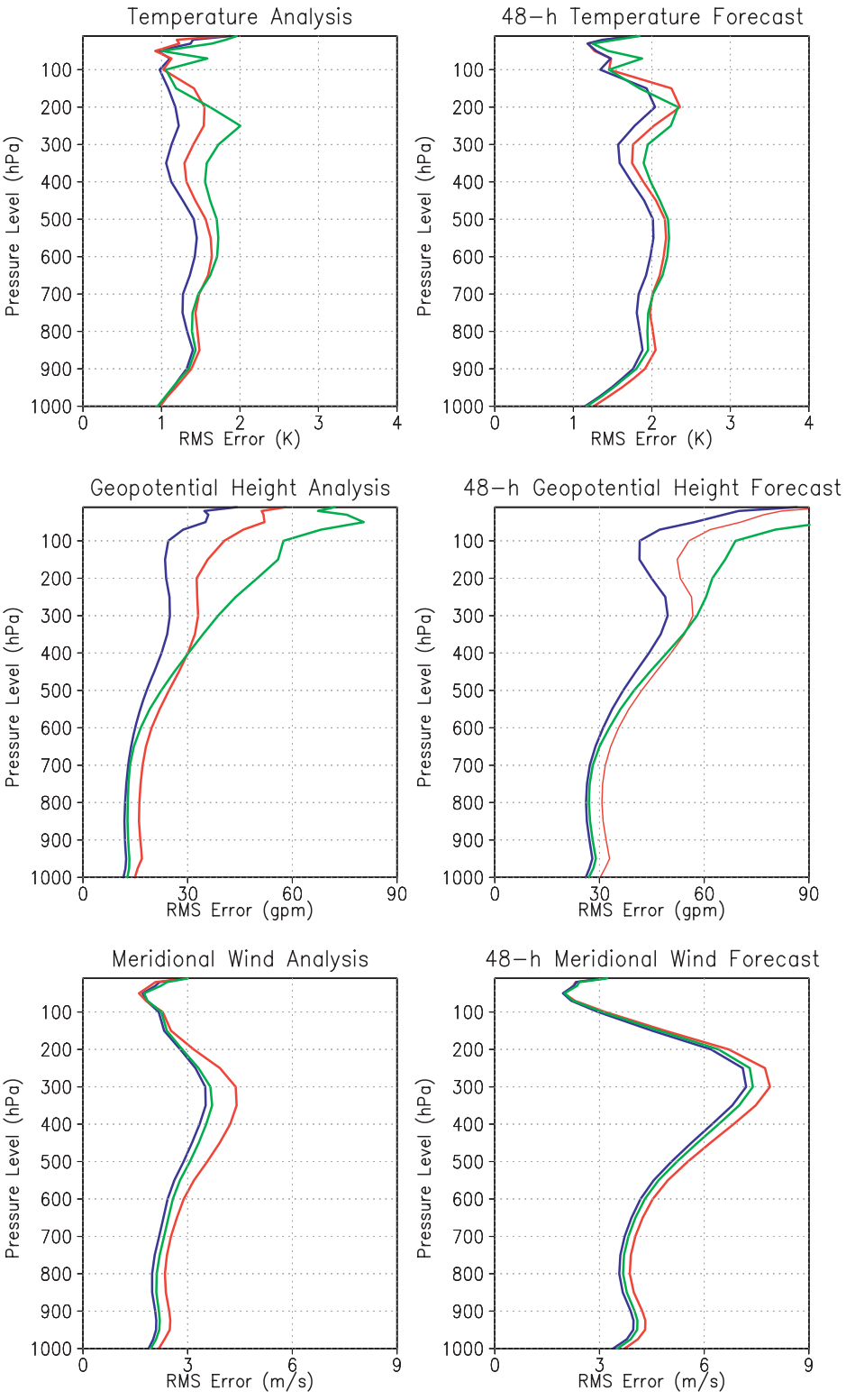

FIG. 5. Time mean of the root-mean-square error, $E_T(p_{g_p})$, at (left) analysis time and (right) 48-h forecast time for different forecast variables in the SH extratropics. Results are show for the experiments with the satellite radiance observations using bias correction (blue), with the satellite radiance observations not using bias correction (green), and without satellite radiance observations (red).

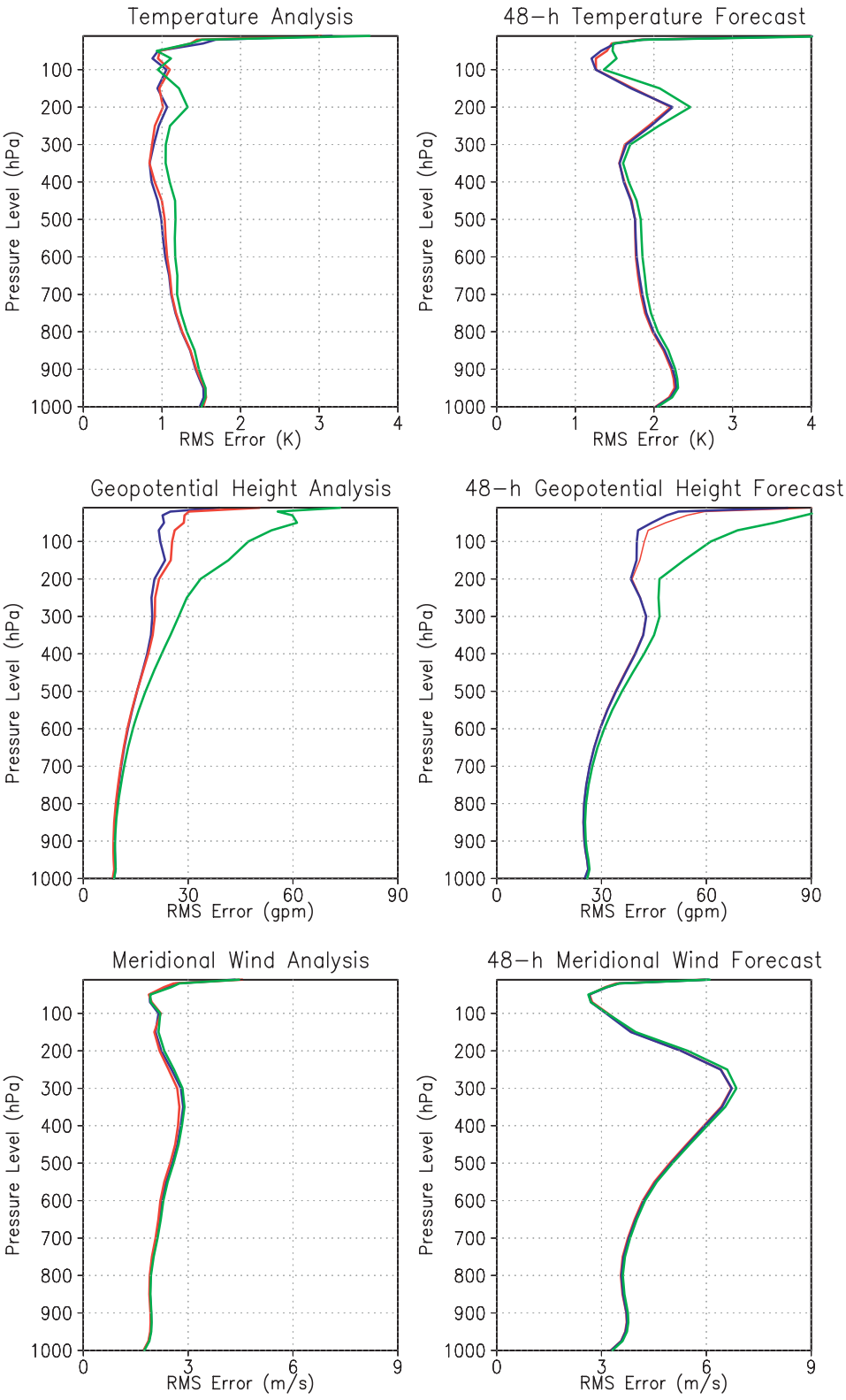

FIG. 6. As in Fig. 5, but for the NH extratropics.

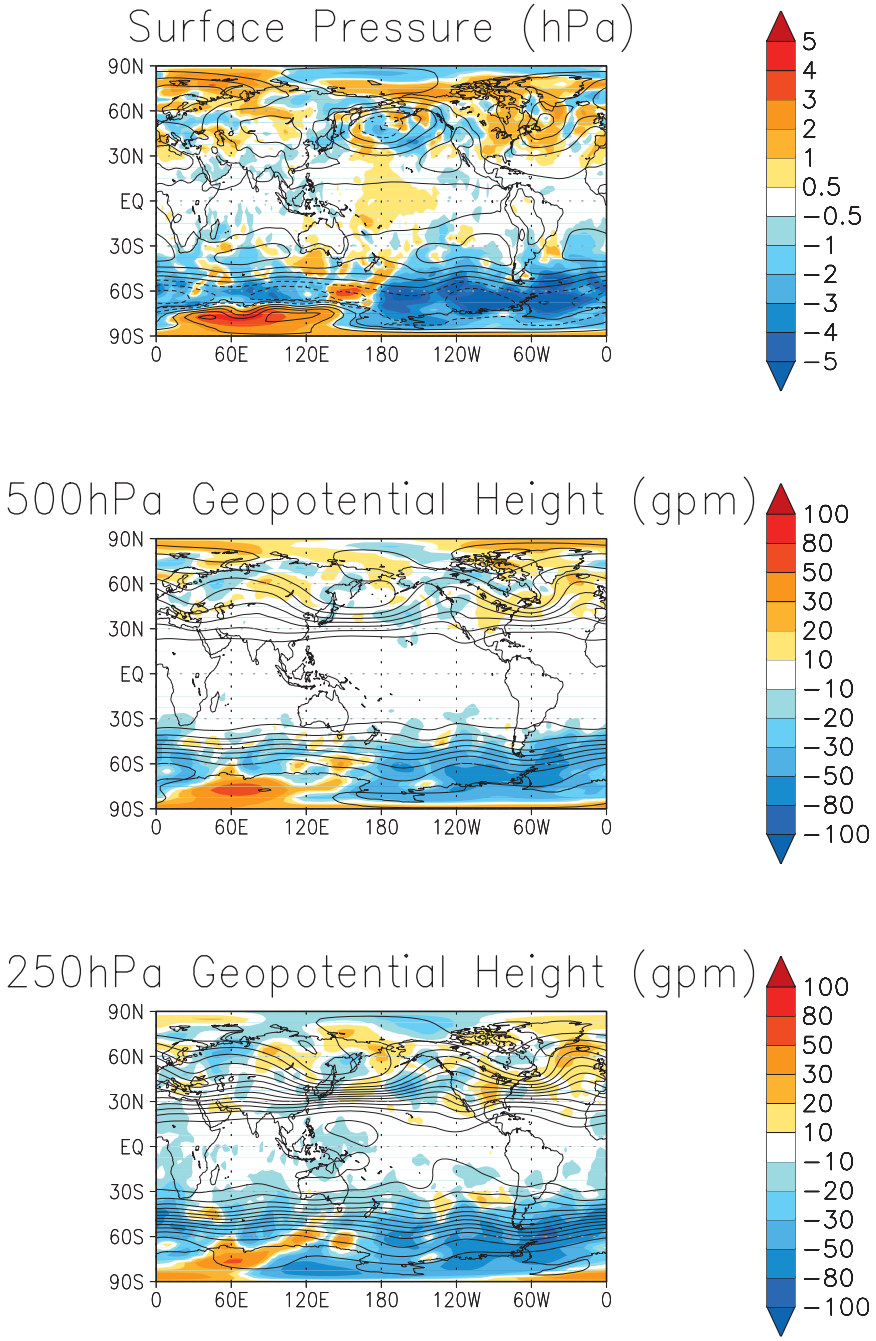

FIG. 7. Color shades show the improvement $I(\lambda_{g_\lambda}, \varphi_{g_\varphi}, p_{g_p})$ in the 48-h forecasts due to the assimilation of AMSU-A observations: (top to bottom) surface pressure, 500 and 200 hPa geopotential height. (Negative values indicate improvement, while positive values indicate degradation.) Contours show the time mean of the verifying analyses.

locations where it is not statistically significant at the 90% level. (We include the figure showing unfiltered results to illustrate the effect of filtering based on statistical significance.) This pair of figures indicates that the analyses are improved over the oceans, with the largest improvement between and east of Cape Horn and the Antarctic Peninsula, while the analyses are degraded over Antarctica. The statistically significant improvement in the surface pressure forecasts indicates that the ensemble-based estimate of the background error covariance matrix provides useful information about the cross correlation between the surface pressure

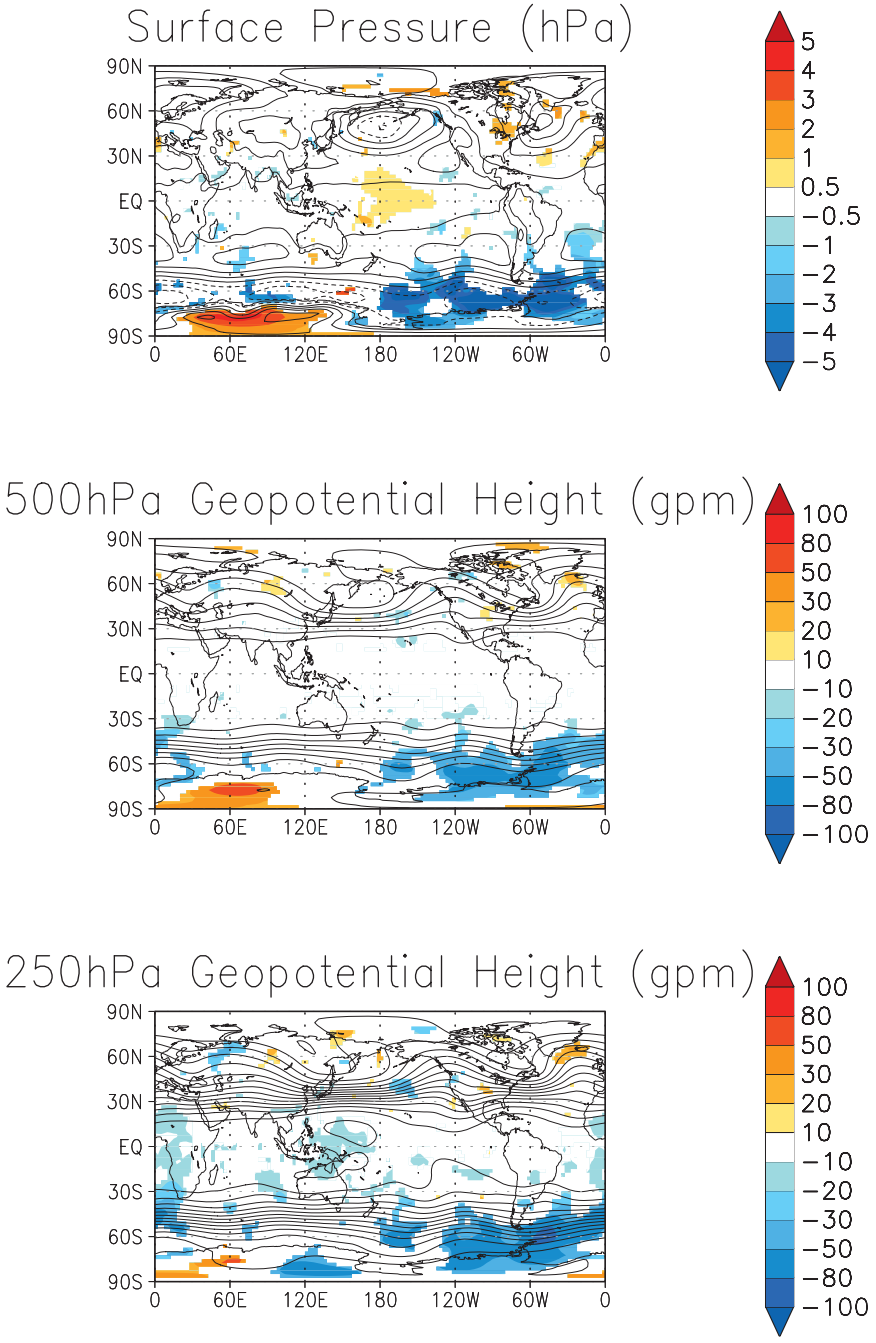

FIG. 8. As in Fig. 7, but that $I(\lambda_{g_\lambda}, \varphi_{g_\varphi}, p_{g_p})$ is shown only at the location where it is significant at the 90% level.

and the atmospheric state variables that directly affect the radiative transfer.

In summary, we can conclude that the assimilation of radiance observations with our proposed strategy is a source of analysis improvement that leads to significant forecast improvement in the SH midlatitudes, which are especially large in the upper troposphere and the stratosphere.

b. The behavior of the bias parameters

To illustrate the behavior of the bias-correction terms, we choose two channels: one that has the average peak sensitivity in the lower troposphere (channel 4) and one that is most sensitive, on average, to the atmospheric conditions in the stratosphere (channel 11). (See Table 2 for typical pressure levels of peak sensitivity for the

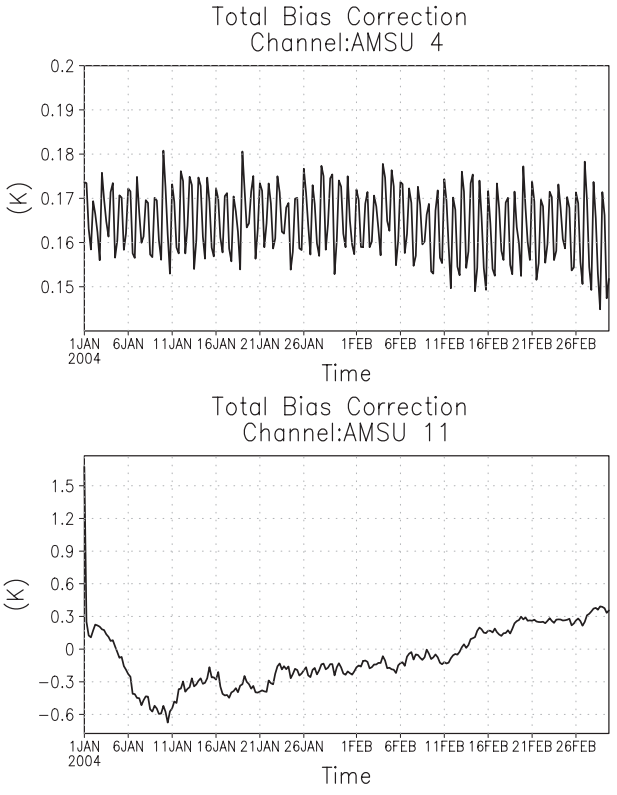

FIG. 9. Time evolution of the estimate of the bias for (top) channel 4 and (bottom) channel 11 in the SH region.

different channels.) We investigate the time evolution of the bias-correction terms for these two channels in the extratropical SH region (Fig. 9).

The time evolution of the bias-correction term is strikingly different for the two channels: while for the channel with peak sensitivity near the surface (channel 4), the time evolution of the bias correction is characterized by a diurnal oscillation around a nearly constant level, for the channel with peak sensitivity in the stratosphere (channel 11), the value of the bias correction shifts from a negative value (about -0.7 K) to a positive value (about 0.3 K). To better understand the behavior of the bias correction, in Fig. 10 we show the contribution of the three predictors (β_j^0, $\beta_j^1 p_1$ and $\beta_j^2 p_2$) to the total bias correction. The results show that the diurnal oscillation in the bias-correction term for channel 4 is due to the oscillation in the term $\beta_j^2 p_2$ associated with the surface temperature predictor β_j^2. In addition, the drift of the value of the bias correction for channel 11 is the net result of a drift of the intercept term $\beta_j^0$and term $\beta_j^2 p_2$ associated with the surface temperature predictor $\beta_j^2 p_2$ in the opposite directions. This shift of the bias-correction terms in the opposite directions suggests that the bias model, which provides an overall good performance for the 8 channels, may not be optimal for channel 11. Except for the scan angle bias component, the magnitude of the bias-correction components is larger for channel 11 than the magnitude of the respective components for channel 4.

Finally, Fig. 11 shows the analysis and the spread of the analysis ensemble for the bias parameters β_j^0 β_j^1, and β_j^2. This figure shows that, for our choices of the variance inflation coefficients ρ and ρ_β, the domain average of the ensemble spread is stable and sufficiently large to allow for continuous changes in the bias parameters. The temporal variability of the bias parameters is clearly larger for channel 11 than for channel 4, indicating that the larger variability in the contribution of the different bias-correction terms observed in Fig. 10 for this channel is the result of changes in the estimates of the bias parameters.

6. Conclusions

In this paper, we tested the techniques developed by Fertig et al. (2007, 2009) for the assimilation of satellite radiance observations in a realistic setting for the first time. The results suggest that the tested strategy can extract useful information about the atmospheric state, especially in regions where the satellite radiance observations are the dominant source of observational information. While our initial results with the ensemble-based bias corrections are promising, several important challenges remain to be addressed. Most importantly, augmenting the local state vector with the bias components significantly increases the dimension of the local state vector (e.g., we added $Q = 24$ extra components to the 4 or 5 components of the state vector in this paper). Since increasing the number of state vector components inevitably increases the dimensionality of the space of uncertainty, we expect that increasing the number of satellite channels will require increasing the number of ensemble members. The fact that we were able to obtain good results without increasing the ensemble size, while increasing the dimension of the local state vector by a factor of 7, is promising for the future, but does not guarantee that the ensemble size would remain manageable in case of a further massive increase of the number of bias parameters.

Our approach for bias correction, which is based on a simultaneous estimation of the state and bias parameters based on an ensemble, is not the only way to estimate and to correct for the bias in the radiance observations in an ensemble-based data assimilation system. Fertig et al. (2009) also introduced, in addition to the algorithm tested here, a two-step approach in which first the bias-correction parameters are estimated with an ensemble-based scheme and then the state is estimated

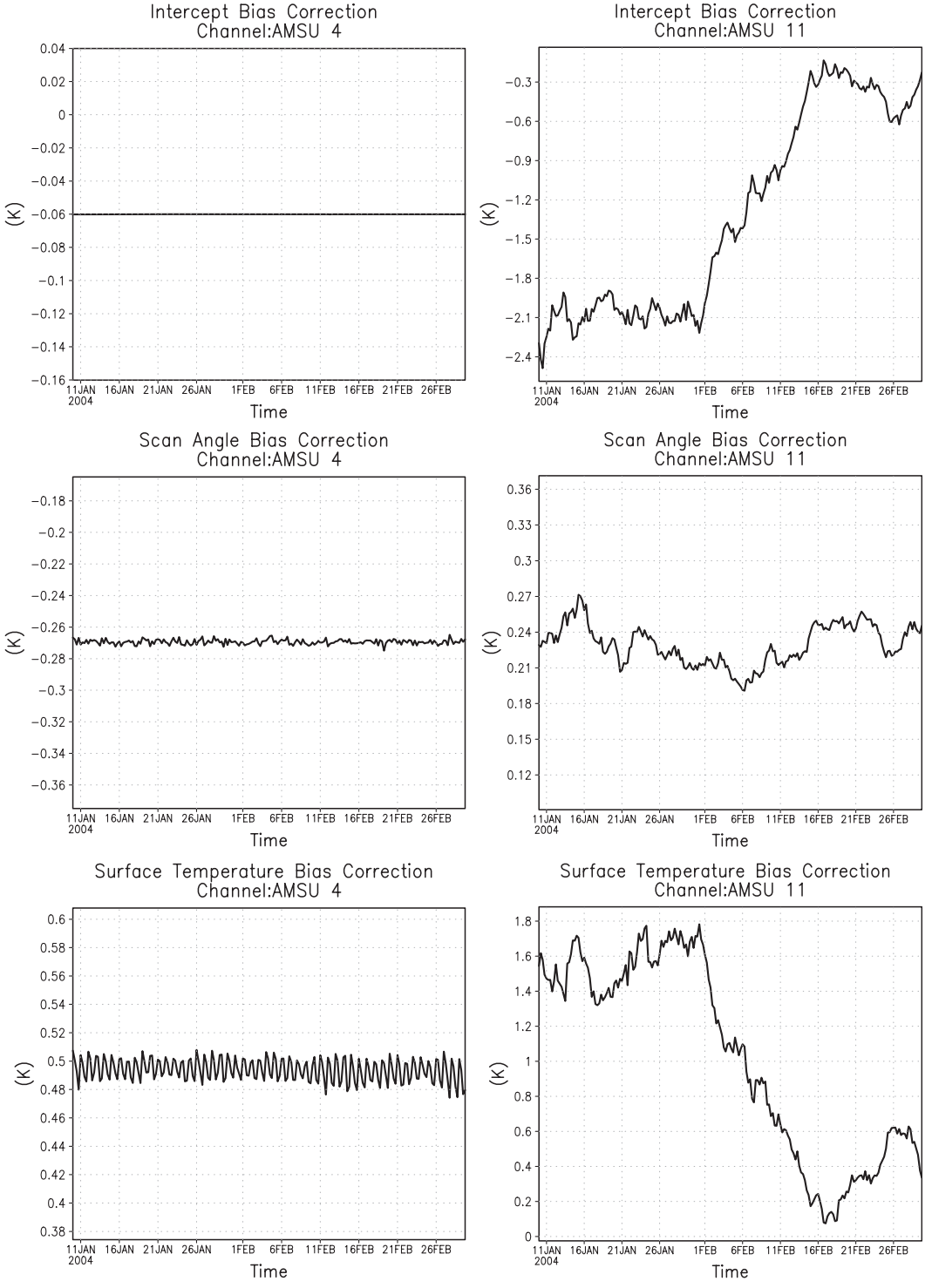

FIG. 10. Time evolution of the bias terms β_j^0, $\beta_j^1 p_1$ and $\beta_j^2 p_2$ for (left) channel 4 and (right) channel 11 in the SH region: (top) intercept, (middle) scan angle bias, and (bottom) surface temperature bias.

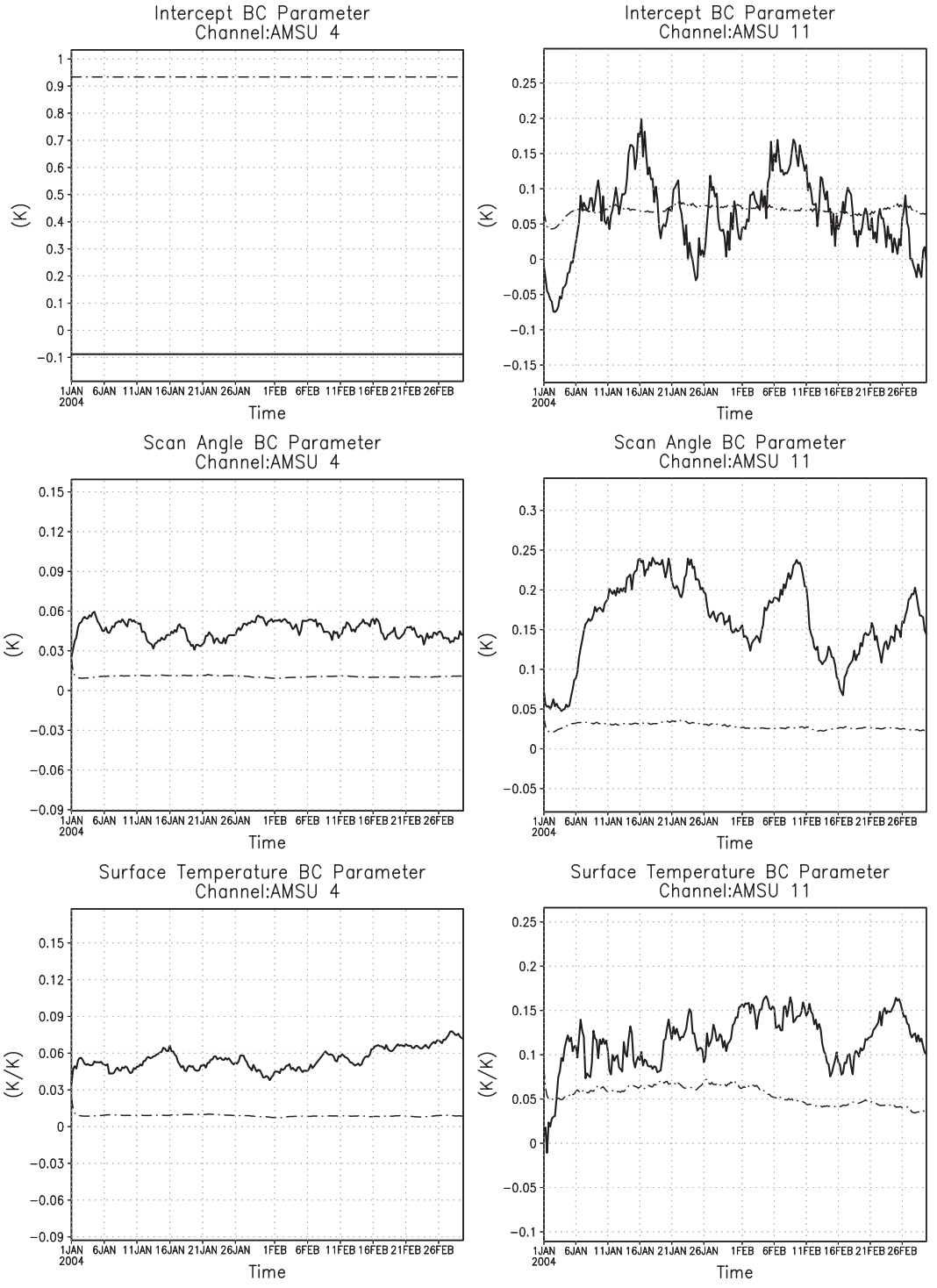

FIG. 11. As in Fig. 10, but for the bias correction parameters β_j^0, β_j^1, and β_j^2 in the SH region (thick solid line). Also shown is the time evolution of the domain average of the spread (standard deviation) of the ensemble of bias parameter estimates (thin dashed line).

in a subsequent step. Moreover, Miyoshi et al. (2010) uses a deterministic approach to obtain a single estimate of each bias parameter simultaneously with the ensemble-based estimate of the atmospheric state. A comparison of the different approaches for observation bias correction in ensemble-based data assimilation systems should be the subject of future research.

Acknowledgments. We thank Ross N. Hoffman of AER, Inc., for his helpful comments on the paper. The thorough reviews by two anonymous reviewers significantly helped to improve the presentation of our results. The work of J. A. on this project was partially funded by the Conselho Nacional de Desenvolvimento Científico e Tecnológico (CNPq, National Council for Scientific and Technological Development of Brazil) under Grants PDE 201185/2005-9 and PU 484245/2006-6. Further funding for this research was provided by NASA (Grants NNX08AD40G, NNX07AV45G, and NNX08AD37G) and NSF (Grants ATM0722721 and ATM0935538).

REFERENCES

Bonavita, M., L. Torrisi, and F. Marcucci, 2008: The ensemble Kalman filter in an operational regional NWP system: Preliminary results with real observations. *Quart. J. Roy. Meteor. Soc.,* **134,** 1733–1744.

Buehner, M., P. L. Houtekamer, C. Charette, H. L. Mitchell, and B. He, 2010a: Intercomparison of variational data assimilation and the ensemble Kalman filter for global deterministic NWP. Part I: Description and single-observation experiments. *Mon. Wea. Rev.,* **138,** 1550–1566.

——, ——, ——, ——, and ——, 2010b: Intercomparison of variational data assimilation and the ensemble Kalman filter for global deterministic NWP. Part II: One-month experiments with real observations. *Mon. Wea. Rev.,* **138,** 1567–1586.

Burgers, G., P.-J. van Leeuwen, and G. Evensen, 1998: Analysis scheme in the ensemble Kalman filter. *Mon. Wea. Rev.,* **126,** 1719–1724.

Campbell, W. F., C. H. Bishop, and D. Hodyss, 2010: Vertical covariance localization for satellite radiances in ensemble Kalman filters. *Mon. Wea. Rev.,* **138,** 282–290.

Dee, D. P., 2005: Bias and data assimilation. *Quart. J. Roy. Meteor. Soc.,* **131,** 3323–3343.

Derber, J. C., and W.-S. Wu, 1998: The use of TOVS cloud-cleared radiances in the NCEP SSI analysis system. *Mon. Wea. Rev.,* **126,** 2287–2299.

Evensen, G., 1994: Sequential data assimilation with a nonlinear quasi-geostrophic model using Monte Carlo methods to forecast error statistics. *J. Geophys. Res.,* **97,** 17 905–17 924.

Eyre, J. R., 1992: A bias correction scheme for simulated TOVS brightness temperatures. Tech. Rep. 186, ECMWF Tech. Memo., 28 pp. [Available from the European Centre for Medium-Range Weather Forecasts, Shinfield Park, Reading, Berkshire R62 9AX, United Kingdom.]

Fertig, E. J., B. R. Hunt, E. Ott, and I. Szunyogh, 2007: Assimilating non-local observations with a local ensemble Kalman filter. *Tellus,* **59A,** 719–730.

——, and Coauthors, 2009: Observation bias correction with an ensemble Kalman filter. *Tellus,* **61A,** 210–226.

Friedland, B., 1969: Treatment of bias in recursive filtering. *IEEE Trans. Automat. Contrib.,* **14,** 359–367.

Han, Y., P. van Delst, Q. Liu, F. Weng, B. Yan, R. Treadon, and J. C. Derber, 2006: JCSDA Community Radiative Transfer Model (CRTM). Tech. Rep. 122, NOAA, 33 pp.

Harris, B. A., and G. Kelly, 2001: A satellite radiance-bias correction scheme for data assimilation. *Quart. J. Roy. Meteor. Soc.,* **127,** 1453–1468.

Houtekamer, P. L., and H. L. Mitchell, 1998: Data assimilation using an ensemble Kalman filter technique. *Mon. Wea. Rev.,* **126,** 796–811.

——, ——, G. Pellerin, M. Buehner, M. Charron, L. Spacek, and B. Hansen, 2005: Atmospheric data assimilation with an ensemble Kalman filter: Results with real observations. *Mon. Wea. Rev.,* **133,** 604–620.

Hunt, B. R., and Coauthors, 2004: Four-dimensional ensemble Kalman filtering. *Tellus,* **56A,** 273–277.

——, E. J. Kostelich, and I. Szunyogh, 2007: Efficient data assimilation for spatiotemporal chaos: A local ensemble transform Kalman filter. *Physica D,* **230,** 112–126.

Miyoshi, T., and Y. Sato, 2007: Assimilating satellite radiances with a Local Ensemble Transform Kalman Filter (LETKF) applied to the JMA global model (GSM). *SOLA,* **135,** 37–40.

——, and S. Yamane, 2007: Local ensemble transform Kalman filtering with an AGCM at a T159/L48 resolution. *Mon. Wea. Rev.,* **135,** 3841–3860.

——, Y. Sato, and T. Kadowaki, 2010: Ensemble Kalman filter and 4D-Var intercomparison with the Japanese operational global analysis and prediction system. *Mon. Wea. Rev.,* **138,** 2846–2866.

Olsen, E. T., 2007: AIRS/AMSU/HSB version 5 data disclaimer. Goddard Space Flight Center, NASA, Jet Propulsion Laboratory, California Institute of Technology, Pasadena, CA, 21 pp. [Available online at http://disc.gsfc.nasa.gov/AIRS/documentation/v5_docs/AIRS_V5_Release_User_Docs/V5_Data_Disclaimer.pdf.]

Ott, E., and Coauthors, 2004: A local ensemble Kalman filter for atmospheric data assimilation. *Tellus,* **56A,** 415–428.

Satterfield, E. A., and I. Szunyogh, 2011: Assessing the performance of an ensemble forecast system in predicting the magnitude and the spectrum of analysis and forecast uncertainties. *Mon. Wea. Rev.,* **139,** 1207–1223.

Szunyogh, I., E. J. Kostelich, G. Gyarmati, D. J. Patil, B. R. Hunt, E. Kalnay, E. Ott, and J. A. Yorke, 2005: Assessing a local ensemble Kalman filter: Perfect model experiments with the National Centers for Environmental Prediction global model. *Tellus,* **57A,** 528–545.

——, ——, ——, E. Kalnay, B. R. Hunt, E. Ott, E. Satterfield, and J. A. Yorke, 2008: A local ensemble transform Kalman filter data assimilation system for the NCEP global model. *Tellus,* **60A,** 113–130.

Torn, R. D., and G. J. Hakim, 2008: Performance characteristics of a pseudo-operational ensemble Kalman filter. *Mon. Wea. Rev.,* **136,** 3947–3963.

Whitaker, J. S., G. P. Compo, X. Wei, and T. M. Hamill, 2004: Reanalysis without radiosondes using ensemble data assimilation. *Mon. Wea. Rev.,* **132,** 1190–1200.

——, T. M. Hamill, X. Wei, Y. Song, and Z. Toth, 2008: Ensemble data assimilation with the NCEP Global Forecast System. *Mon. Wea. Rev.,* **136,** 463–482.

Wilks, D. S., 2006: *Statistical Methods in the Atmospheric Sciences*. 2nd ed. Academic Press, 627 pp.